Dynamic screening of quasiparticles in WS$_2$ monolayers

Stefano Calati

Humboldt-Universität zu Berlin, Institut für Chemie, and Fritz-Haber-Institut der Max-Planck-Gesellschaft,
Abt. Physikalische Chemie, Berlin, Germany

Qiuyang Li

Department of Chemistry, Columbia University, New York, New York 10027, USA

Xiaoyang Zhu

Department of Chemistry, Columbia University, New York, New York 10027, USA

Julia Stähler [*]

Humboldt-Universität zu Berlin, Institut für Chemie, and Fritz-Haber-Institut der Max-Planck-Gesellschaft,
Abt. Physikalische Chemie, Berlin, Germany

We unravel the influence of quasiparticle screening in the nonequilibrium exciton dynamics of monolayer WS$_2$. We report pump photon energy-dependent exciton blue- and redshifts from time-resolved-reflectance contrast measurements. Based on a phenomenological model, we isolate the effective impact of excitons and free carriers on the renormalization of the quasifree particle band gap, exciton binding energy, and linewidth broadening. By this, our work not only provides a comprehensive picture of the competing phenomena governing the exciton dynamics in WS$_2$ upon photoexcitation, but also demonstrates that exciton and carrier contributions to dynamic screening of the Coulomb interaction differ significantly.

I. INTRODUCTION

Excitons in two-dimensional materials attracted substantial interest in fundamental science [1] and are highly relevant for future technological applications [2]. Particularly, transition metal dichalcogenides (TMDCs) exhibit, due to their two-dimensional nature, a reduced screening of the Coulomb interaction (CIA), which governs the excitonic properties: binding energies on the order of the hundreds of meV [3], the quasifree particle band gap, and, thus, the resonance energy of the exciton. The environment [4], preparation technique [5], defect density [5], temperature [6], and doping [7] can change the screening of the CIA and, therefore, change the optical properties of the material. When the system is driven out of equilibrium, photoexcited quasiparticles (i.e., excitons or quasifree carriers) further modify the electronic structure by renormalization [8–17] through *dynamic* screening of the CIA. Due to the complexity of these phenomena, previous studies focused on specific aspects and investigated them in depth. However, a comprehensive picture of the mechanisms contributing to the dynamic exciton response in TMDCs was not reported yet, and the detailed impact of different types of photoexcited quasiparticles on the exciton dynamics is still to be understood. For instance, enhanced screening of free carriers and excitons may reduce the exciton binding energy as well as the quasifree particle band gap, potentially leading to both blue- and redshifts of the exciton resonance.

Although both quasiparticle species act on the screening of the CIA, it is *a priori* not clear whether their impact on binding energy and quasifree carrier band gap is similarly strong, as carriers and excitons show different degrees of (de-)localization and, thus, polarizability. This work disentangles the influence of exciton and quasifree carrier (QFC) screening on the nonequilibrium dynamics of the exciton resonance. We employ time-resolved optical pump-probe broadband reflectance contrast (tr-RC) to investigate the pump energy- and fluence-dependent response of the A exciton resonance of a monolayer of WS$_2$ upon photoexcitation. We selectively create excitons or QFC by photoexciting in and above resonance of the A exciton, respectively. Then, we determine the time-dependent dielectric function of the exciton as introduced previously [18], tracking its peak shift and broadening. These dynamics are then fitted using a simple model description of the transient quasiparticle populations, showing excellent agreement with the data and providing material parameters in line with the literature. Based on this, we conclude that the linewidth broadening is dominated by QFC-exc and exc-exc scattering. QFC screening induces a redshift of the A exciton due to band gap renormalization (BGR) being the dominant effect, while exciton screening leads to a blueshift caused by a strong exciton binding-energy reduction. These findings demonstrate that, despite the fact that both quasiparticle types enhance the screening of the CIA, screening by excitons has a very different effect on the exciton resonance energy than carrier screening. This is likely a consequence of their different polarizability and localization. The
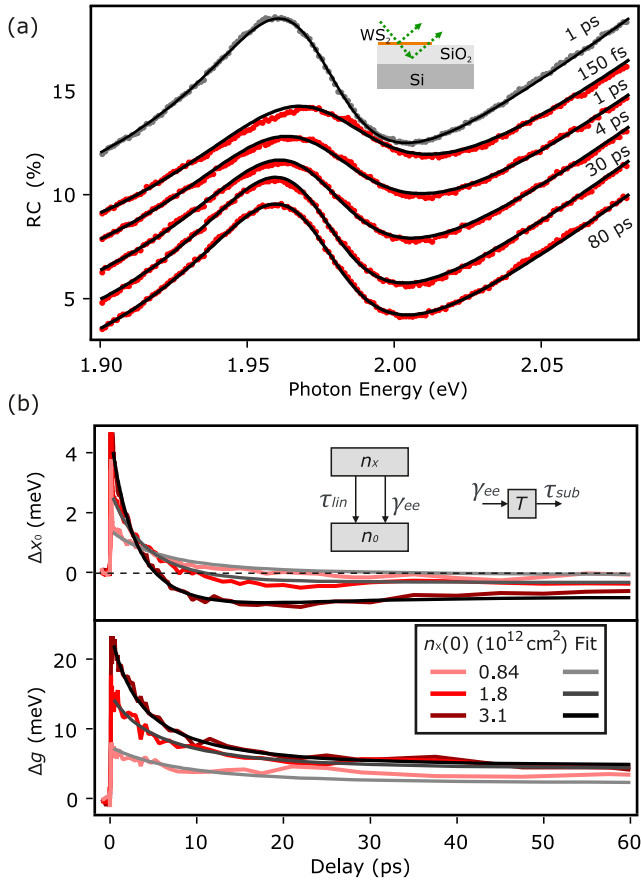
---
[*]Corresponding author: julia.staehler@hu-berlin.de

FIG. 1. (a) RC spectra (colored markers) for selected delays with fits (gray traces) for an initial exciton density of $n_x(0) = 3.1 \times 10^{12}$ cm^{-2}. Traces are vertically shifted for clarity. (b) Time-dependent exciton peak shift (Δx_0) and broadening (Δg) dynamics for different fluences for resonant pumping. Corresponding fits using Eqs. (5) and (3). Inset: Sketch of the two-level model.

model reported in this work, even though it is restricted to the most basic mechanisms, constitutes the first quantitative and comprehensive description of the competing phenomena governing the transient optical properties of WS$_2$. This sets a basis for a quantitative comparison of existing and future experimental studies to extract reliable material properties and parameters. Ultimately, this model can be extended to include more complex interactions in TMDC materials.

II. EXPERIMENTAL

We study a monolayer of WS$_2$ on a silicon wafer covered with a thin layer (285 nm) of SiO$_2$ as sketched in the inset of Fig. 1(a) using time-resolved reflectance contrast (tr-RC). We chose the commonly used [7,8,10] Si/SiO$_2$ as a substrate in order to ensure comparability of our results to previous data. Furthermore, it guarantees a high contrast between the monolayer and the bare substrate. A first pump laser pulse at 1.98 or 3.1 eV perturbs the system, and a broadband white light probe pulse [19] monitors the reflectance contrast RC = $(R_{sub} - R_{sub+WS_2})/R_{sub}$ as a function of the delay t between pump and probe pulses. The experimental details

are described in the Supplemental Material [20] (see, also, Refs. [19,21,22] therein).

III. RESULTS

A. Resonant excitation

Figure 1(a) shows RC spectra for a few selected pump-probe delays for resonant excitation of the A exciton (1.98 eV). The negative time delay ($t = -1$ ps; gray) RC spectrum is the steady-state spectrum. The A exciton signature undergoes peak shift and broadening upon photoexcitation. We model the RC spectrum with a Lorentz oscillator and the Fresnel transfer matrix formalism [23] to account for reflections at the multiple interfaces of the sample, as presented in a previous publication [18]. Fits of each spectrum are displayed in Fig. 1(a), excellently agreeing with the data. With this approach, we extract the time-dependent exciton peak shift $\Delta x_0 = x_0(t) - x_0(eq)$, linewidth broadening $\Delta g = g(t) - g(eq)$, and spectral weight change at different pump fluences, as displayed in Fig. 1(b). We observe an abrupt blueshift of the resonance upon photoexcitation. The blueshift ($\Delta x_0 > 0$) turns into a redshift ($\Delta x_0 < 0$) at larger delays; the sooner, the higher the pump fluence (cf. crossing of the traces with the dashed zero line). Furthermore, we observe a broadening persisting for tens of picoseconds after photoexcitation (bottom panel). The spectral weight does not change within the noise level of our measurements (see Supplemental Material [20]).

Note that when the pump photon energy is tuned into resonance with the exciton, only excitons are photoexcited initially [13]. Based on this, we describe the A exciton dynamics in the simplest way, assuming a phenomenological two-level model sketched in the inset of Fig. 1(b). The pump generates an initial photoexcited exciton density $n_x(0) = n_{hv}$ (with n_{hv} the number of absorbed photons) calculated from the pump fluence and spectrum as described in [18] and in the Supplemental Material [20] (see, also, Refs. [24–27] therein). The excitons relax to the ground state n_0 through a linear recombination channel [28] (with a rate $1/\tau_{lin}$) and a quadratic term that is likely attributed to Auger recombination [29] with the rate $\gamma_{e\text{-}e}$. The time-dependent exciton population density n_x is retrieved by solving

$$\frac{dn_x}{dt} = -\frac{1}{\tau_{lin}}n_x - \gamma_{e\text{-}e}n_x^2. \tag{1}$$

Importantly, the Auger recombination induces energy transfer from the electronic to the phonon system, ultimately increasing the lattice temperature and resulting in a redshift of the exciton [10]. We assume that the lattice temperature increase is proportional to $\gamma_{e\text{-}e}n_x^2$, the rate of exciton Auger recombination times the square of the exciton density, as all nonradiatively dissipated energy eventually ends up in the phonon bath. This is sketched in the inset of Fig. 1(b). The excess thermal energy of the lattice is dissipated to the substrate with a rate $1/\tau_{sub}$. The temperature evolution $T(t)$ is given by

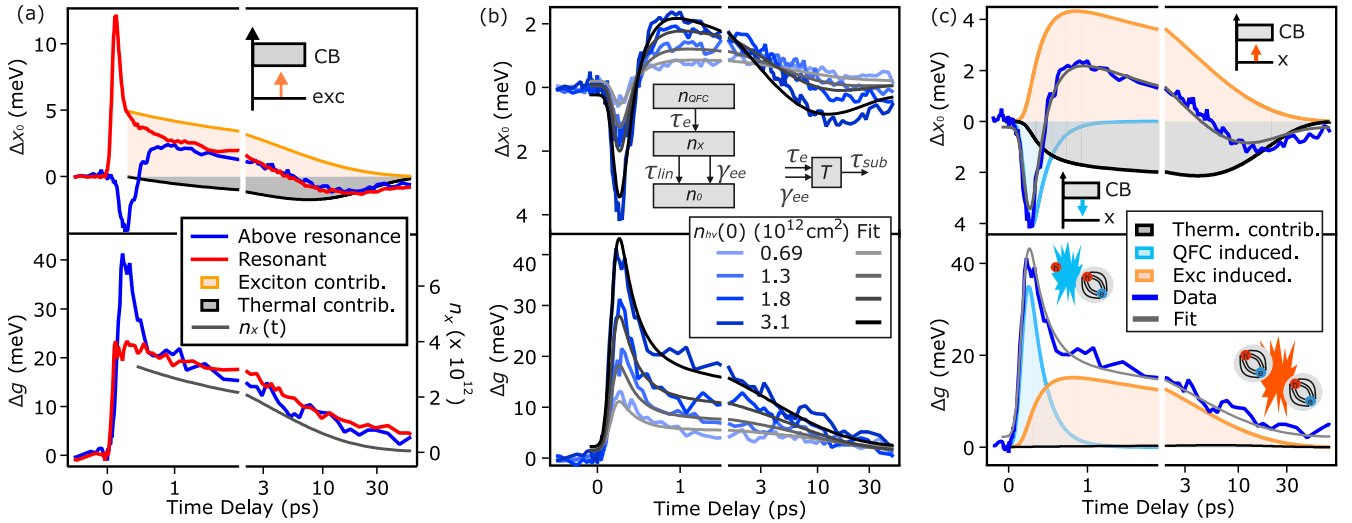$$\frac{dT(t)}{dt} = +\gamma_{e\text{-}e}n_x^2 \frac{x_0(eq)}{\rho c_p d} - \frac{1}{\tau_{sub}}T \tag{2}$$

FIG. 2. (a) Time-dependent exciton peak shift (Δx_0) and broadening (Δg) for above-resonance (blue) and resonant (red) pumping with an absorbed photon density $n_{hv}(0) = 3.1 \times 10^{12}$ cm^{-2}. Binding-energy reduction (orange solid) and temperature-induced (solid gray) contributions to resonant peak-shift dynamics. The time-dependent exciton density $n_x(t)$ is displayed on the right axis of the bottom panel. (b) Above-resonance pumping: time-dependent exciton peak shift and broadening for different fluences with corresponding fit using Eqs. (10) and (9). Inset: sketch of the three-level model. (c) Top panel: Time-dependent exciton peak shift for above-resonance pumping and corresponding fit with Eq. (10) [from panel (b)]. Time-dependent contributions to the peak shift originating from temperature increase (gray), QFC (light blue), and excitons (orange). Bottom panel: photoinduced broadening and respective fit with Eq. (9) from panel (b). Contribution to the broadening from QFC-exc (light blue) and exc-exc scattering (orange).

with the bulk WS$_2$ density $\rho = 7.5$ g/cm^3 [10], the specific heat $c_p = 0.25$ J/gK [10], and the height of the monolayer $d = 0.7$ nm measured with atomic force microscopy (AFM; see Supplemental Material [20]).

We now relate the exciton peak shift $\Delta x_0(t)$ and broadening $\Delta g(t)$ to the time-dependent lattice temperature increase and the exciton density n_x. In a first approach, it can be assumed that the broadening is proportional to the scattering events between excitons, corresponding to a collisional broadening picture. The broadening is linear in the density of photoexcited quasiparticles [30], leading to

$$\Delta g(t) = n_x D \tag{3}$$

with an excitation-induced broadening parameter D.

For the description of the exciton peak shift, we assume the binding energy to be equal to the work needed to bring the electron to an infinite distance from the hole in a screened environment, given by the formula

$$E_B(t) = \frac{e^2}{4\pi r_0 \varepsilon_0 \left[\varepsilon_{r_s} + \varepsilon_{r_{\mathrm{dyn}}}(t)\right]}, \tag{4}$$

where e is the elementary charge, ε_0 is the vacuum dielectric constant, and r_0 is the distance between the electron and the hole forming the exciton, approximated to the Bohr radius of 1 nm [11]. The relative permittivity consists of a static term ε_{r_s} attributed to the effective screening of the dielectric environment. We fix it to the average of the relative permittivity of SiO$_2$ ($\varepsilon_r = 3.9$) and air $\varepsilon_{r_s} = 2.45$. The second, dynamic term $\varepsilon_{r_{\mathrm{dyn}}}(t) = \alpha n_x(t)$ is proportional to the exciton density through the coefficient α and describes the dynamic screening of other excitons. The exciton resonance energy is then given by the

following expression:

$$\Delta x_0(t) = E_B(eq) - E_B[n_x(t)] + \beta \Delta T(t). \tag{5}$$

Here, the last term describes the temperature-induced redshift based on Eq. (2) and $E_b(eq)$ is given by Eq. (4) for $\varepsilon_{r_{\mathrm{dyn}}} = 0$.

We now test the accuracy of this model by performing a global fit to the fluence-dependent peak shift and broadening with the functions Eqs. (5) and (3), respectively. We start by fitting the experimental curves 150 fs after time zero, where we can assume an incoherent exciton population [31]. The dynamics during the presence of the pump pulse are not analyzed to avoid resonant processes such as the optical Stark effect [32,33]. The fit results are shown in Fig. 1(b). The excellent agreement between the fit and the extracted peak shift and broadening confirms that this simple model can reproduce the exciton dynamics for excitation densities below the Mott transition. This includes the reproduction of the initial blueshift by the exciton density-dependent binding energy, the following redshift due to the temperature rise, and, remarkably, the broadening that is simply proportional to n_x.

Based on this excellent agreement, we deduce that the restriction to the essential mechanisms and simple population considerations are sufficient to describe all aspects of the photoinduced dynamics in monolayer WS$_2$ upon resonant photoexcitation. These mechanisms are (i) exc-exc scattering as the primary source of the photoinduced broadening, as shown by the similar trend of broadening and $n_x(t)$ in the bottom panel of Fig. 2(a), (ii) dynamic screening of excitons inducing binding-energy reduction and, thus, the blueshift at early time delays, and (iii) the temperature increase due to the Auger recombination leading to the observed redshift at later time delays. The relative contributions of exciton screening and temperature-induced shift are displayed in Fig. 2(a)

(top). Their competition determines the absolute shift of the exciton. For low initial excited quasiparticle densities, the thermally induced redshift is minimal due to the fact that excitons recombine prevalently through the linear recombination channel. Instead, the higher the initial photoexcitation density, the higher is the fraction of excitons recombining by Auger recombination, thus leading to an increase in temperature.

To further test the robustness of this model, the same analysis was performed on transmittance contrast data taken on a monolayer WS$_2$ placed on a fused silica substrate, finding that the model accurately reproduces the dynamics also in this independent experiment (see Supplemental Material [20]) (see, also, Refs. [18,34]). The model thus describes the effects of excitons on the optical observables independent of sample, measurement technique, and substrate.

B. Above-resonance excitation

Before discussing the extracted fit parameters, we focus on the role of the QFC. We perform the same tr-RC experiment, but using a pump of 3.1 eV photon energy. This initially generates quasifree electrons and holes in the system instead of excitons as in the resonant pumping scheme. It is expected that, after they have released their excess energy by scattering processes, they form bound electron-hole pairs [35]. Any difference that is observed in the data of this experiment compared to the resonant pumping case will thus be a result of the QFC in the system. As above, we extract the time-dependent Δx_0 and Δg from the tr-RC using the Fresnel transfer matrix formalism [18,23].

Figure 2(a) compares exciton peak shift and broadening for resonant (red) and above-resonance (blue) pumping with the same initial absorbed photon density. The data clearly shows differing dynamics during the first picosecond after photoexcitation. An initial blue- and redshift is observed for the resonant and above-resonance pumping, respectively. Additionally, a stronger broadening of the exciton resonance is present for above-resonance pumping. The dynamics at later times overlap across the whole delay range after the above-resonance pumping redshift turns rapidly into a blueshift, and the broadening relaxes quickly to values similar to the resonant pumping case. Qualitatively, the same is observed for the other excitation densities [Fig. 2(b)].

The initially differing dynamics must result from the initial QFC population that subsequently decays into an exciton population with the corresponding equilibration dynamics. To quantify this, we extend the phenomenological model by introducing a third level for the QFC population, as depicted in the inset of Fig. 2(b). The initial QFC density $n_{QFC}(0) = 2n_{h\nu}$ relaxes by forming excitons at a rate of $1/\tau_e$;

$$\frac{dn_{QFC}(t)}{dt} = -\frac{1}{\tau_e}n_{QFC}. \qquad (6)$$

Due to the quick nature of the exciton formation process, the exponential decay resulting from solving this rate equation is convoluted with a Gaussian to account for the laser pulses' cross correlation. This gives an analytical expression of $n_{QFC}(t)$. The time-dependent exciton population $n_x(t)$ becomes

$$\frac{dn_x(t)}{dt} = +\frac{1}{\tau_e}\frac{n_{QFC}}{2} - \frac{1}{\tau_{lin}}n_x - \gamma_{e\text{-}e}n_x^2, \qquad (7)$$

where the first term is the exciton population build-up taking into account that an exciton is formed by two QFCs. The remaining terms are analogous to Eq. (1).

The relaxation of hot QFC forming excitons also yields an additional temperature rise [36]. We approximate that the QFC excess energy $h\nu_{pump} - x_0(eq)$ is transferred to the lattice at the same rate $1/\tau_e$ as the excitons are being formed. Inserting this into Eq. (2), we obtain

$$\frac{dT(t)}{dt} = \frac{1}{\tau_e}n_{h\nu}\frac{h\nu_{pump} - x_0(eq)}{\rho c_p d} + \gamma_{e\text{-}e}n_x^2\frac{x_0(eq)}{\rho c_p d} - \frac{1}{\tau_{sub}}T. \qquad (8)$$

We solve Eqs. (7) and (8) numerically, thus providing the time-dependent exciton density and lattice temperature.

To relate the three-level model to the observed broadening, another broadening channel must be added to Eq. (3), corresponding to the QFC-exc scattering:

$$\Delta g(t) = n_x D + n_{QFC}K. \qquad (9)$$

Here, K is the excitation-induced broadening parameter for QFC-exc scattering.

To model the QFC induced peak shift, we assume that the QFC effectively induces a redshift due to BGR caused by enhanced screening, in line with the clear experimental result that the resonance initially redshifts when QFCs are present. We assume this redshift to be linear in n_{QFC} within the limited fluence range of this work:

$$\Delta x_0(t) = E_B(eq) - E_B[n_x(t)] + \beta \Delta T(t) - E_{QFC}n_{QFC}. \qquad (10)$$

We globally fit the fluence-dependent exciton position and broadening for the above-resonance pumping with Eqs. (10) and (9), keeping the shared parameters extracted from the resonant pumping data fixed. The fits are shown in Fig. 2(b), displaying an excellent agreement with the complex dynamics. Despite being a simplification, this model captures the global redshift of the exciton resonance caused by BGR through QFC screening, and the broadening of the exciton resonance through QFC-exc scattering. Note that our model reproduces the linewidth broadening without including a thermal contribution [cf. Eq. (9)], different compared to previous works [10,37].

IV. DISCUSSION AND CONCLUSION

We now turn to the parameters extracted from the global fitting, reported in Table I. The timescales of the relaxation processes occurring after photoexcitation: exciton formation time τ_e, Auger recombination rate $\gamma_{e\text{-}e}$, and thermal energy transfer to the substrate τ_{sub} are consistent with values previously reported [10,38–42], even specifying the values within the ranges reported in literature. Notably, the expression for the transient temperatures [Eqs. (2) and (8)] were able to reproduce the slower dynamics without having to include temperature changes due to the linear exciton recombination channel (τ_{lin}). This suggests radiative electron-hole recombination, trapping, or dark exciton formation that do not transfer significant amounts of energy to the lattice. Reported values

TABLE I. Best-fit parameters of the model.

τ_e (fs)	200 ± 10	$\leqslant 1000$ [38]
τ_{lin} (ps)	18 ± 5	
γ_{e-e} (cm^2/s)	0.06 ± 0.01	0.05–0.1 [39–42]
τ_{sub} (ps)	14 ± 8	ps-μs [10,43,44]
β (meV/K)	0.4 ± 0.1	0.25–0.5 [10]
α (cm^2)	$(6.6 \pm 0.6) \times 10^{-15}$	
E_{QFC} (meV cm^2)	$(1.2 \pm 0.1) \times 10^{-12}$	
D (meV cm^2)	$(5.6 \pm 0.2) \times 10^{-12}$	5.4×10^{-12} [30]
K (meV cm^2)	$(9.8 \pm 0.2) \times 10^{-12}$	

for radiative recombination vary quite drastically from subpicoseconds to nanoseconds [45–47] and also defect trapping of the excitons, as predicted [45] and measured [48] previously for MoS$_2$ and WSe$_2$, respectively, as well as dark exciton formation [47] for WSe$_2$ occur on timescales consistent with τ_{lin}.

The temperature-induced shift coefficient β, lies within the values reported in literature [10,43,44]. The excitation-induced broadening parameter for exc-exc scattering D is also consistent with the literature value [30], and the one for QFC-exc scattering K is expected to be higher than D due to higher mobility and lower effective mass of QFC [49], in agreement with our observation. The consistency of all these parameters with the literature values shows that the model is based on appropriate assumptions and that the most essential mechanisms influencing the exciton resonance dynamics are an accurate description of the dominating processes.

The remaining two parameters, E_{QFC} and α, were not reported in the literature before. While the former determines the redshift of the exciton resonance induced by QFC screening [cf. Eq. (10)], the latter causes the blueshift induced by exciton screening that enhances the relative permittivity [cf. Eq. (4)]. In order to quantitatively compare the QFC and exciton-induced shifts, we simplify the exciton-induced binding-energy reduction to $\Delta E(t) = E_X n_x(t)$, which is possible, as $\varepsilon_{\text{dyn}}(t) \ll \varepsilon_s$. Here, the proportionality factor $E_X = [E_B(eq) \alpha / \varepsilon_s] = 1.6 \times 10^{12}$ meV/cm^2 expresses the net exciton screening contribution to the binding-energy reduction. It can be directly compared to the value of $E_{\text{QFC}} = 1.2 \times 10^{12}$ meV/cm^2, which quantifies the effective redshift induced by quasifree electron-hole pairs.

While both, exciton and QFC shifts, are a result of the competing processes of binding-energy reduction and BGR through screening of the two quasiparticle types, they have *opposite* signs, despite the fact that excitons are composed of electron-hole pairs, as the QFC population. The origin of this opposing screening effect, must, therefore, lie in the different screening of bound versus unbound electron-hole pairs. It seems highly likely that the very different degree of localization of the bound electron-hole pairs that extend across a few lattice sites and the delocalized character of electrons and holes in the quasifree carrier bands is causing this phenomenon. Presumably, the spatially well-separated excitons simply have a negligible impact on the self-energy of the system and do not cause any relevant BGR. The QFC, conversely, affects the band gap significantly, as generally observed in semiconductors, and this effect is exceeding any

carrier-induced binding-energy reduction, leading to an effective redshift.

The opposite sign and a comparison of the magnitude of the respective resonance shifts of carriers and excitons is illustrated in Fig. 2(c) The figure depicts the time-dependent exciton peak shift (top) and broadening (bottom), and respective fits, for an above-resonance pumping tr-RC dataset with an initial absorbed photon density of $n_{h\nu}(0) = 3.1 \times 10^{12}$ cm^{-2}. The QFC and exciton contributions to shift and broadening are displayed in light blue and orange, respectively. Initially, the redshift ($\Delta x < 0$; light blue) due to QFC dominates and decays quickly with the exciton formation time $\tau_e = 200$ fs. The resulting build-up of exciton population then causes an increasing blueshift ($\Delta x > 0$; orange). At the same time, the temperature-induced BGR ($\Delta x < 0$; black) rises, as the relaxation of carriers heats up the lattice. After roughly half a picosecond, the sum of all these shifts Δx (dark blue) equals zero: more than half of the carrier population has turned into excitons.

The similar magnitude of QFC and exciton screening-induced blue and redshifts is likely the cause for the varying observations in the literature [8–17], as excitation density and photon energy have a significant impact on this fragile balance. We hope that our simple model will prove useful in interpreting and understanding of previous and future experimental results on the dynamics in WS$_2$ as well as other two-dimensional systems with reduced static screening.

V. SUMMARY

The pump fluence- and photon-energy-dependent quasiparticle dynamics of monolayer WS$_2$ were studied by means of time-resolved reflectance contrast. Excitons and quasifree carriers were selectively photoexcited in the system employing resonant/above-resonance optical pumping. We showed that a very reduced model describing QFC and exciton population dynamics is able to reproduce the dynamics of the exciton resonance upon photoexcitation fully, including several crossover regions, while providing parameters in excellent agreement with the literature. Based on this, the photoexcited quasiparticles' effective impact on the exciton dynamics is unveiled. QFCs induce broadening of the exciton resonance through QFC-exc scattering and a redshift of the resonance by BGR. Excitons, instead, induce broadening of the resonance through exc-exc scattering and a blueshift modeled by binding-energy reduction. Remarkably, our model quantifies the screening-induced contributions of carriers and excitons to the overall shift of the exciton resonance, which are very similar, but with opposite signs, likely due to the different degree of localization of the two quasiparticle species. This work provides a basic, but still accurate and comprehensive picture of the competing phenomena that govern the exciton dynamics in WS$_2$ upon photoexcitation, guaranteeing a common ground for comparing experimental studies of TMDCs and the extraction of reliable material properties and parameters. Furthermore, the two-/three-level model may serve as a base for possible extensions to include more complex interactions in TMDC materials, maybe even at higher excitation densities above the Mott limit.

[1] G. Wang, A. Chernikov, M. M. Glazov, T. F. Heinz, X. Marie, T. Amand, and B. Urbaszek, *Colloquium*: Excitons in atomically thin transition metal dichalcogenides, Rev. Mod. Phys. **90**, 021001 (2018).

[2] D. Jariwala, V. K. Sangwan, L. J. Lauhon, T. J. Marks, and M. C. Hersam, Emerging device applications for semiconducting two-dimensional transition metal dichalcogenides, ACS Nano **8**, 1102 (2014).

[3] B. Zhu, X. Chen, and X. Cui, Exciton binding energy of monolayer WS_2, Sci. Rep. **5**, 9218 (2015).

[4] W.-T. Hsu, J. Quan, C.-Y. Wang, L.-S. Lu, M. Campbell, W.-H. Chang, L.-J. Li, X. Li, and C.-K. Shih, Dielectric impact on exciton binding energy and quasiparticle bandgap in monolayer WS_2 and WSe_2, 2D Mater. **6**, 025028 (2019).

[5] B. Kaviraj and D. Sahoo, Physics of excitons and their transport in two dimensional transition metal dichalcogenide semiconductors, RSC Adv. **9**, 25439 (2019).

[6] J. Huang, T. B. Hoang, and M. H. Mikkelsen, Probing the origin of excitonic states in monolayer WSe_2, Sci. Rep. **6**, 22414 (2016).

[7] A. Chernikov, A. M. van der Zande, H. M. Hill, A. F. Rigosi, A. Velauthapillai, J. Hone, and T. F. Heinz, Electrical Tuning of Exciton Binding Energies in Monolayer WS_2, Phys. Rev. Lett. **115**, 126802 (2015).

[8] P. D. Cunningham, A. T. Hanbicki, K. M. McCreary, and B. T. Jonker, Photoinduced bandgap renormalization and exciton binding energy reduction in WS_2, ACS Nano **11**, 12601 (2017).

[9] E. J. Sie, A. Steinhoff, C. Gies, C. H. Lui, Q. Ma, M. Rösner, G. Schönhoff, F. Jahnke, T. O. Wehling, Y.-H. Lee, J. Kong, P. Jarillo-Herrero, and N. Gedik, Observation of exciton redshift–blueshift crossover in monolayer WS_2, Nano Lett. **17**, 4210 (2017).

[10] C. Ruppert, A. Chernikov, H. M. Hill, A. F. Rigosi, and T. F. Heinz, The role of electronic and phononic excitation in the optical response of monolayer WS_2 after ultrafast excitation, Nano Lett. **17**, 644 (2017).

[11] A. Chernikov, C. Ruppert, H. M. Hill, A. F. Rigosi, and T. F. Heinz, Population inversion and giant bandgap renormalization in atomically thin WS_2 layers, Nat. Photon. **9**, 466 (2015).

[12] E. A. A. Pogna, M. Marsili, D. De Fazio, S. Dal Conte, C. Manzoni, D. Sangalli, D. Yoon, A. Lombardo, A. C. Ferrari, A. Marini, G. Cerullo, and D. Prezzi, Photo-induced bandgap renormalization governs the ultrafast response of single-layer MoS_2, ACS Nano **10**, 1182 (2016).

[13] A. Steinhoff, M. Florian, M. Rösner, G. Schönhoff, T. O. Wehling, and F. Jahnke, Exciton fission in monolayer transition metal dichalcogenide semiconductors, Nat. Commun. **8**, 1166 (2017).

[14] M. Selig, F. Katsch, R. Schmidt, S. Michaelis de Vasconcellos, R. Bratschitsch, E. Malic, and A. Knorr, Ultrafast dynamics in monolayer transition metal dichalcogenides: Interplay of dark excitons, phonons, and intervalley exchange, Phys. Rev. Res. **1**, 022007(R) (2019).

[15] C. Trovatello, F. Katsch, N. J. Borys, M. Selig, K. Yao, R. Borrego-Varillas, F. Scotognella, I. Kriegel, A. Yan, A. Zettl, P. J. Schuck, A. Knorr, G. Cerullo, and S. D. Conte, The ultrafast onset of exciton formation in 2D semiconductors, Nat. Commun. **11**, 5277 (2020).

[16] Z. E. Eroglu, O. Comegys, L. S. Quintanar, N. Azam, S. Elafandi, M. Mahjouri-Samani, and A. Boulesbaa, Ultrafast dynamics of exciton formation and decay in two-dimensional tungsten disulfide (2D-WS_2) monolayers, Phys. Chem. Chem. Phys. **22**, 17385 (2020).

[17] Y. Lin, Y.-H. Chan, W. Lee, L.-S. Lu, Z. Li, W.-H. Chang, C.-K. Shih, R. A. Kaindl, S. G. Louie, and A. Lanzara, Exciton-driven renormalization of quasiparticle band structure in monolayer MoS_2, Phys. Rev. B **106**, L081117 (2022).

[18] S. Calati, Q. Li, X. Zhu, and J. Stähler, Ultrafast evolution of the complex dielectric function of monolayer WS_2 after photoexcitation, Phys. Chem. Chem. Phys. **23**, 22640 (2021).

[19] D. Wegkamp, D. Brida, S. Bonora, G. Cerullo, J. Stähler, M. Wolf, and S. Wall, Phase retrieval and compression of low-power white-light pulses, Appl. Phys. Lett. **99**, 101101 (2011).

[20] See Supplemental Material at http://link.aps.org/supplemental/10.1103/PhysRevB.107.115404 for details on data analysis and additional data.

[21] S. B. Desai, S. R. Madhvapathy, M. Amani, D. Kiriya, M. Hettick, M. Tosun, Y. Zhou, M. Dubey, J. W. Ager III, D. Chrzan, and A. Javey, Gold-mediated exfoliation of ultralarge optoelectronically-perfect monolayers, Adv. Mater. **28**, 4053 (2016).

[22] F. Liu, M. E. Ziffer, K. R. Hansen, J. Wang, and X. Zhu, Direct Determination of Band-Gap Renormalization in the Photoexcited Monolayer MoS_2, Phys. Rev. Lett. **122**, 246803 (2019).

[23] O. Stenzel, *The Physics of Thin Film Optical Spectra* (Springer-Verlag, Berlin, Heidelberg, 2005).

[24] I. H. Malitson, Interspecimen comparison of the refractive index of fused silica, J. Opt. Soc. Am. **55**, 1205 (1965).

[25] D. E. Aspnes and A. A. Studna, Dielectric functions and optical parameters of Si, Ge, GaP, GaAs, GaSb, InP, InAs, and InSb from 1.5 to 6.0 eV, Phys. Rev. B **27**, 985 (1983).

[26] N. C. Passler, M. Jeannin, and A. Paarmann, Layer-resolved absorption of light in arbitrarily anisotropic heterostructures, Phys. Rev. B **101**, 165425 (2020).

[27] N. Ansari and F. Ghorbani, Light absorption optimization in two-dimensional transition metal dichalcogenide van der Waals heterostructures, J. Opt. Soc. Am. B **35**, 1179 (2018).

[28] L. Yuan and L. Huang, Exciton dynamics and annihilation in WS_2 2D semiconductors, Nanoscale **7**, 7402 (2015).

[29] D. Sun, Y. Rao, G. A. Reider, G. Chen, Y. You, L. Brézin, A. R. Harutyunyan, and T. F. Heinz, Observation of rapid exciton–exciton annihilation in monolayer molybdenum disulfide, Nano Lett. **14**, 5625 (2014).

[30] G. Moody, C. Kavir Dass, K. Hao, C.-H. Chen, L.-J. Li, A. Singh, K. Tran, G. Clark, X. Xu, G. Berghäuser, E. Malic, A. Knorr, and X. Li, Intrinsic homogeneous linewidth and broadening mechanisms of excitons in monolayer transition metal dichalcogenides, Nat. Commun. **6**, 8315 (2015).

[31] M. Selig, G. Berghäuser, M. Richter, R. Bratschitsch, A. Knorr, and E. Malic, Dark and bright exciton formation, thermalization, and photoluminescence in monolayer transition metal dichalcogenides, 2D Mater. **5**, 035017 (2018).

[32] P. D. Cunningham, A. T. Hanbicki, T. L. Reinecke, K. M. McCreary, and B. T. Jonker, Resonant optical Stark effect in monolayer WS$_2$, Nat. Commun. **10**, 5539 (2019).

[33] E. J. Sie, J. W. McIver, Y.-H. Lee, L. Fu, J. Kong, and N. Gedik, Valley-selective optical Stark effect in monolayer WS$_2$, Nat. Mater. **14**, 290 (2015).

[34] Y. Li and T. F. Heinz, Two-dimensional models for the optical response of thin films, 2D Mater. **5**, 025021 (2018).

[35] F. Ceballos, Q. Cui, M. Z. Bellus, and H. Zhao, Exciton formation in monolayer transition metal dichalcogenides, Nanoscale **8**, 11681 (2016).

[36] F. Caruso, Nonequilibrium lattice dynamics in monolayer MoS$_2$, J. Phys. Chem. Lett. **12**, 1734 (2021).

[37] M. Selig, G. Berghäuser, A. Raja, P. Nagler, C. Schüller, T. F. Heinz, T. Korn, A. Chernikov, E. Malic, and A. Knorr, Excitonic linewidth and coherence lifetime in monolayer transition metal dichalcogenides, Nat. Commun. **7**, 13279 (2016).

[38] P. Steinleitner, P. Merkl, P. Nagler, J. Mornhinweg, C. Schüller, T. Korn, A. Chernikov, and R. Huber, Direct observation of ultrafast exciton formation in a monolayer of WSe$_2$, Nano Lett. **17**, 1455 (2017).

[39] Y. Yu, Y. Yu, C. Xu, A. Barrette, K. Gundogdu, and L. Cao, Fundamental limits of exciton-exciton annihilation for light emission in transition metal dichalcogenide monolayers, Phys. Rev. B **93**, 201111(R) (2016).

[40] P. D. Cunningham, K. M. McCreary, and B. T. Jonker, Auger recombination in chemical vapor deposition-grown monolayer WS$_2$, J. Phys. Chem. Lett. **7**, 5242 (2016).

[41] S. Han, C. Boguschewski, Y. Gao, L. Xiao, J. Zhu, and P. H. M. van Loosdrecht, Incoherent phonon population and exciton-exciton annihilation dynamics in monolayer WS$_2$ revealed by time-resolved resonance Raman scattering, Opt. Express **27**, 29949 (2019).

[42] Y. Fu, D. He, J. He, A. Bian, L. Zhang, S. Liu, Y. Wang, and H. Zhao, Effect of dielectric environment on excitonic dynamics in monolayer WS$_2$, Adv. Mater. Interfaces **6**, 1901307 (2019).

[43] H.-L. Liu, T. Yang, J.-H. Chen, H.-W. Chen, H. Guo, R. Saito, M.-Y. Li, and L.-J. Li, Temperature-dependent optical constants of monolayer MoS$_2$, MoSe$_2$, WS$_2$, WSe$_2$: spectroscopic ellipsometry and first-principles calculations, Sci. Rep. **10**, 15282 (2020).

[44] W. Zhao, R. M. Ribeiro, M. Toh, A. Carvalho, C. Kloc, A. H. Castro Neto, and G. Eda, Origin of indirect optical transitions in few-layer MoS$_2$, WS$_2$, and WSe$_2$, Nano Lett. **13**, 5627 (2013).

[45] H. Wang, J. H. Strait, C. Zhang, W. Chan, C. Manolatou, S. Tiwari, and F. Rana, Fast exciton annihilation by capture of electrons or holes by defects via Auger scattering in monolayer metal dichalcogenides, Phys. Rev. B **91**, 165411 (2015).

[46] G. Moody, J. Schaibley, and X. Xu, Exciton dynamics in monolayer transition metal dichalcogenides, J. Opt. Soc. Am. B **33**, C39 (2016).

[47] C. Poellmann, P. Steinleitner, U. Leierseder, P. Nagler, G. Plechinger, M. Porer, R. Bratschitsch, C. Schüller, T. Korn, and R. Huber, Resonant internal quantum transitions and femtosecond radiative decay of excitons in monolayer WSe$_2$, Nat. Mater. **14**, 889 (2015).

[48] Q. Cui, F. Ceballos, N. Kumar, and H. Zhao, Transient absorption microscopy of monolayer and bulk WSe$_2$, ACS Nano **8**, 2970 (2014).

[49] A. Honold, L. Schultheis, J. Kuhl, and C. W. Tu, Collision broadening of two-dimensional excitons in a GaAs single quantum well, Phys. Rev. B **40**, 6442 (1989).